Coherent control of NV⁻ centers in diamond in a quantum teaching lab

Vikas K. Sewani, Hyma H. Vallabhapurapu, Yang Yang, Hannes R. Firgau, Chris Adambukulam, Brett C. Johnson, Jarryd J. Pla, and Arne Laucht

---

ARTICLES YOU MAY BE INTERESTED IN

AAPT 2021
PHYSICS EDUCATION®

VIRTUAL SUMMER MEETING | July 31 – August 4

INSTRUCTIONAL LABORATORIES AND DEMONSTRATIONS

The downloaded PDF for any Note in this section contains all the Notes in this section.

John Essick, *Editor*

Department of Physics, Reed College, Portland, OR 97202

Articles in this section deal with new ideas and techniques for instructional laboratory experiments, for demonstrations, and for equipment that can be used in either. Although these facets of instruction also appear in regular articles, this section is for papers that primarily focus on equipment, materials, and how they are used in instruction. Manuscripts should be submitted using the web-based system that can be accessed via the *American Journal of Physics* home page, ajp.aapt.org, and will be forwarded to the IL&D editor for consideration.

Coherent control of NV⁻ centers in diamond in a quantum teaching lab

Vikas K. Sewani,[a)] Hyma H. Vallabhapurapu, Yang Yang, and Hannes R. Firgau
Centre for Quantum Computation and Communication Technology, School of Electrical Engineering and Telecommunications, UNSW Sydney, Sydney, New South Wales 2052, Australia

Chris Adambukulam
School of Electrical Engineering and Telecommunications, UNSW Sydney, Sydney, New South Wales 2052, Australia

Brett C. Johnson
Centre for Quantum Computation and Communication Technology, School of Physics, University of Melbourne, Melbourne, Victoria 3010, Australia

Jarryd J. Pla
School of Electrical Engineering and Telecommunications, UNSW Sydney, Sydney, New South Wales 2052, Australia

Arne Laucht[b)]
Centre for Quantum Computation and Communication Technology, School of Electrical Engineering and Telecommunications, UNSW Sydney, Sydney, New South Wales 2052, Australia

The room temperature compatibility of the negatively charged nitrogen-vacancy (NV⁻) center in diamond makes it the ideal quantum system for a university teaching lab. Here, we describe a low-cost experimental setup for coherent control experiments on the electronic spin state of the NV⁻ center. We implement spin-relaxation measurements, optically detected magnetic resonance, Rabi oscillations, and dynamical decoupling sequences on an ensemble of NV⁻ centers. The relatively short times required to perform each of these experiments (<10 min) demonstrate the feasibility of the setup in a teaching lab. Learning outcomes include basic understanding of quantum spin systems, magnetic resonance, the rotating frame, Bloch spheres, and pulse sequence development.

I. INTRODUCTION

The arrival of the second quantum revolution—technologies that exploit coherent quantum phenomenon, such as quantum computation, quantum communication, and quantum sensors—has elevated quantum physics from fundamental research to an applied science.[1] A thorough understanding of quantum mechanics is not only desirable but quite often demanded of university graduates entering the job market in this field. Theoretical skills are easily taught with pen and paper, by deriving analytical solutions, or with a few lines of computer code running numerical simulations, but real hands-on experience in manipulating a quantum system is, unfortunately, much more difficult to convey. This is partly due to the sensitivity of quantum systems to environmental disturbances that often demands operation at cryogenic temperatures or inside vacuum chambers, and partly due to the high cost of specialized equipment.

The NV⁻ center in diamond is an especially advantageous quantum system for a teaching lab as its electron spins can be initialized, controlled, and read out at room temperature in ambient atmosphere,[2] strongly reducing the complexity of the experimental apparatus. Hence it has previously been recommended for teaching lab setups for magnetic resonance and magnetometry by Zhang *et al*. in Ref. 3, and is even available as a commercial system.[4] While the experimental apparatus required to extend the experiments to coherent control is more complex, it has been thoroughly described in literature by Bucher *et al*. in Ref. 5. However, coherent control has not been

demonstrated in a convenient and cost-effective fashion targeted at a university teaching lab.

Here, we describe a teaching lab setup that allows students to learn about fundamental concepts of quantum mechanics by coherently controlling the electronic spin state of the NV$^-$ center in diamond. In fact, students can adapt and design their own control sequences and experiments. The presented setup is robust to its environmental conditions, such that it can even be operated in broad daylight on a normal desk, and does not require the carefully controlled environment of a research laboratory. Finally, the setup can be assembled for a total cost of less than USD 20k.

This paper is organized as follows: in Sec. II, we will give an overview of the learning outcomes that can be conveyed with these experiments. In Sec. III, we will give a short introduction to the NV$^-$ center in diamond, explaining how initialization, control, and readout of the electronic spin states is achieved. Section IV provides a detailed description of the experimental setup. More specifically, Sec. IV A describes the diamond sample we use, Sec. IV B describes the optical part of the setup, Sec. IV C describes the equipment required for delivery of a microwave (MW) field, and Sec. IV D describes the signal detection scheme using a lock-in amplifier in combination with digital pulse sequences. Finally, Sec. V discusses the various experiments that can be conducted with this setup, with special attention to the quantum mechanical concepts that these experiments convey.

II. LEARNING OUTCOMES

At UNSW Sydney, the experiments described below have been incorporated into a course targeted at the 4th-year undergraduate level. At the time of writing, we have thus far run the course for one semester in which students have been able to successfully perform all experiments, and demonstrate the learning outcomes. A total of nine students were enrolled in that semester, and were divided into groups of two or three. Each group had two hours per week to perform the experiments, for four weeks in total. Due to the number of groups, two identical setups were built and were operated simultaneously during the lab times. Throughout the course of the labs, it was essential for students to demonstrate links between experimental results, and both quantitative and qualitative understanding of quantum theory. More specifically, these labs encourage students to achieve the following:

(1) Understand the NV$^-$ center structure, the spin initialization and readout procedure, and the spectral features.
(2) Incrementally develop pulse sequences with increasing complexity, i.e., starting from purely optical spin-dynamics for T_1 measurements, up to complex dynamical decoupling sequences for T_2 measurements.
(3) Understand the rotating frame, magnetic resonance, two-axes control, and be able to follow the spin orientations along the Bloch sphere during pulse sequences.
(4) Understand the incremental steps required to implement dynamical decoupling pulse sequences, such as finding a spin transition in the spectrum, performing Rabi oscillations, and calibrating π-pulse lengths. Due to the short experimental run times, students can often perform all experiments in a single two-hour lab once they have obtained the expertise.

Concepts demonstrated with these experiments are transferable to other quantum systems,[6] like electron spin qubits confined to donors or quantum dots,[7,8] nuclear spin qubits,[9] superconducting qubits,[10] atoms in ion traps,[11] and magnetic resonance imaging (MRI).[12] Literature that is readily available on these systems frequently benchmarks quantum devices using the same methods as described below. Performing such experiments has, up until now, often only been available to research students in an expensive research lab.

III. THE NV$^-$ CENTER IN DIAMOND

The NV$^-$ center in diamond consists of a substitutional nitrogen atom adjacent to a vacant lattice site, as schematically shown in Fig. 1(a). It can exist along four different crystallographic orientations ([111], [1$\bar{1}\bar{1}$], [$\bar{1}$1$\bar{1}$], and [$\bar{1}\bar{1}$1]), which are in principle equivalent, but lead to different alignments of their NV$^-$ center axes with respect to an externally applied static or oscillating magnetic field.

The static Hamiltonian of the NV$^-$ center ground state, neglecting any interactions with nuclear spins or spin-strain interactions, and assuming that the NV$^-$-axis is oriented along the z-direction, is given by

$$\mathcal{H}_0 = DS_z^2 + \gamma_e B_0 S_u, \tag{1}$$

where $D = 2.87$ GHz is the zero-field splitting of the ground state, $\gamma_e = 28$ GHz/T is the electron gyromagnetic ratio, B_0 is the magnetic field applied along an arbitrary direction $\vec{u}$, and $S_{x,y,z,u}$ are the spin matrices for $S = 1$ along the x,y,z-axes and the $\vec{u}$-direction.[13] In this paper, we will treat $\mathcal{H}_0$ in units of frequency, as this is more relevant for the experiments.

In order to achieve magnetic spin resonance and coherent control, we need an oscillating magnetic field B_1 that induces transitions between the spin sublevels. For example, a resonant B_1 field enables us to controllably rotate the ground state spin states from $|0\rangle$ to $|\pm1\rangle$ and back (termed *Rabi oscillations*). This field is usually created at the position of the NV$^-$ centers using a MW signal generator and an antenna (discussed further in Sec. IV). We include the
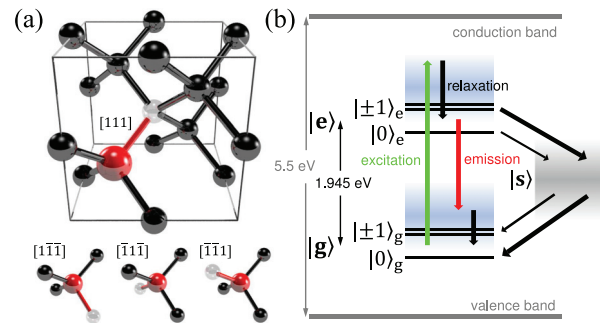
Fig. 1. (Color online) (a) Atomic structure of the NV center in diamond with a substitutional nitrogen atom adjacent to a vacant lattice site. The depicted NV center is oriented along the [111] lattice direction, however, due to the tetrahedral structure of the crystal lattice, the NV center axis can also be oriented along the [1$\bar{1}\bar{1}$], [$\bar{1}$1$\bar{1}$], and [$\bar{1}\bar{1}$1] lattice directions. (b) Energy levels and transitions of the NV$^-$, with ground state $|g\rangle$, excited state $|e\rangle$, and intermediate singlet states $|s\rangle$. The corresponding shaded regions represent continua of orbital and vibrational states. Thicker arrows represent high probability transitions, while thinner arrows represent low probability transitions.

oscillating magnetic field in the Hamiltonian as a time-dependent term given by

$$\mathcal{H}_1 = \gamma_e B_1 \cos(2\pi\nu_1 t)S_v, \qquad (2)$$

where B_1 is the magnitude of the oscillating magnetic field at frequency ν_1 applied along an arbitrary direction $\vec{v}$, and S_v is the spin matrix along the $\vec{v}$-direction.

Due to the exact way the sample is mounted in the setup, there can be an angle between the static magnetic field B_0, the oscillating magnetic field B_1, and the direction in which the crystal field acts [defined as the z-direction in Eq. (1)], as for example indicated in Fig. 4(d). In fact, due to the four possible orientations of the NV$^-$ center axis in the tetrahedral crystal, NV$^-$ centers with different orientations will, intrinsically, have different Zeeman splittings and Rabi frequencies.

The experiments described in this paper will only be concerned with the spin physics of the ground state described above, denoted $|g\rangle$ in Fig. 1(b). However, in order to describe the spin initialization and readout mechanisms, we must consider the optically excited state $|e\rangle$ and the intermediate singlet states $|s\rangle$, also depicted in Fig. 1(b). The ground state $|g\rangle$ and excited state $|e\rangle$ are both spin-carrying states with $S = 1$. In $|g\rangle$ at $B_0 = 0$ T, the $|\pm 1\rangle_g$ states are at $\nu_D = 2.87$ GHz higher energy than the $|0\rangle_g$ state due to the zero-field splitting D. Green laser light at $\lambda = 520$ nm or $\lambda = 532$ nm can excite the NV$^-$ electrons from the ground state $|g\rangle$ into the continuum of orbital and vibrational excited states (shaded region near $|e\rangle$) above the excited state $|e\rangle$ (referred to as off-resonant excitation), from which they rapidly relax into $|e\rangle$. From there the electrons can decay radiatively, either directly to $|g\rangle$ by emitting a photon at $\lambda_{\text{ZPL}} = 637$ nm into the zero-phonon-line (ZPL), or by simultaneously emitting a phonon and a photon of longer wavelength into the phonon-sideband (PSB). In either case, there is a high probability that the spin state of the electron will remain unchanged during this optical cycling, due to spin-conservation. Alternatively, the NV$^-$ electrons can decay nonradiatively via the singlet state $|s\rangle$. Decay from $|e\rangle$ to $|s\rangle$ is favoured by the $|\pm 1\rangle_e$ states compared to the $|0\rangle_e$ state (as indicated by the thicker arrow), and decay from $|s\rangle$ to $|g\rangle$ favours the $|0\rangle_g$ spin orientation of $|g\rangle$. Overall, these transition rules have two effects:

(1) Electrons cycling between the $|0\rangle_g$ and $|0\rangle_e$ states emit $\sim 30\%$ more photons than those cycling between the $|\pm 1\rangle_g$ and $|\pm 1\rangle_e$ states. This provides a readout mechanism for the ensemble electronic spin state.
(2) With continuous laser excitation, electrons cycling between $|\pm 1\rangle_g$ and $|\pm 1\rangle_e$ states will over time populate the $|0\rangle_g$ state. The electrons can therefore be spin-initialized into the $|0\rangle_g$ state.[2]

IV. EQUIPMENT

In this section, we provide details about the experimental setup. All optical and electrical components were purchased off-the-shelf, while the printed circuit boards for the antenna [see Fig. 2(c)] and the laser current driver (more information in Appendix B) can be commercially manufactured (*Eagle CAD* files are included in the supplementary material).[15] A detailed list of all parts with part numbers and recent prices can be found in Appendix A.

A. Diamond sample

The diamond sample is a single crystal Type 1b $\langle 111 \rangle$-oriented high-pressure, high-temperature (HPHT) diamond obtained from *Sumitomo*. In order to obtain a high NV$^-$ concentration, the diamond was additionally electron-irradiated in-house with a density of 10^{18} electrons/cm^2, and annealed in vacuum at $900\,^\circ$C for 2 h. The electron irradiation significantly increases the PL intensity but reduces the coherence times,[16] which can be a limiting factor for some more advanced measurement protocols. All experiments measure the photoluminescence (PL) from a large ensemble of NV$^-$ centers with all four possible orientations. While the sample used in this manuscript requires some processing, a $\langle 100 \rangle$-oriented HPHT diamond sample with high NV$^-$ center density of a few ppm can be purchased from *Scimed*,[17] and a $\langle 100 \rangle$-oriented chemically vapour-deposited (CVD) diamond sample (available from *Element Six*)[18] is also sufficient for the experiments described herein and will contain a measurable number of NV$^-$ centers, without any additional processing. In Appendix C, we show a comparison between the HPHT diamond that was used for the experiments in this manuscript and the commercially available CVD diamond from *Element Six* for a zero-field spin resonance experiment (as in Sec. V B) and a Rabi experiment (as in Sec. V C). The CVD sample has a ~ 1000 times lower PL signal, and while the spin signal decreases proportionally, we obtain high-quality data with only ~ 10 times longer measurement times. In contrast, the CVD sample has a much longer coherence time than the HPHT sample that allows observation of effects originating from coupling to nuclear spins (not discussed in this work). The effect of the different crystal orientations with respect to the diamond surface on our experiment is described in Sec. V C and Ref. 19.

B. Optical setup

The setup was designed with the goal of keeping the optical components to a minimum while ensuring ease of alignment. This way, the setup can be easily incorporated onto a small optical breadboard (Thorlabs MB3045/M) for portability, and fully covered with an enclosure (Thorlabs XE25C7/M) to constrain laser scattering.

A schematic of the optics part of our setup is shown in Fig. 2(b). We use a single mode, fiber-coupled 520 nm green laser diode (Thorlabs LP520-SF15) as our excitation source. The beam is first collimated using an aspheric lens (Thorlabs C280TMD-A), and then reflected off a 550 nm long-pass dichroic mirror (Thorlabs DMLP550) and onto a microscope objective (Olympus MS Plan $50\times$/0.80NA). The objective lens focuses the laser to a focal spot of ~ 1 μm on the diamond sample, which results in an excitation volume over which B_0 and B_1 field are both relatively constant. The diamond sample is mounted on a 3-axis translation stage (Thorlabs MBT616D/M). Between the objective lens and the diamond sample, we place a printed circuit board (PCB) MW antenna to create the strong oscillating magnetic field (B_1 field) for spin control. The antenna structure includes a 1 mm diameter hole, through which both the excitation laser and the PL emission from the diamond sample can pass. The design of the antenna is discussed in more detail in Sec. IV C.
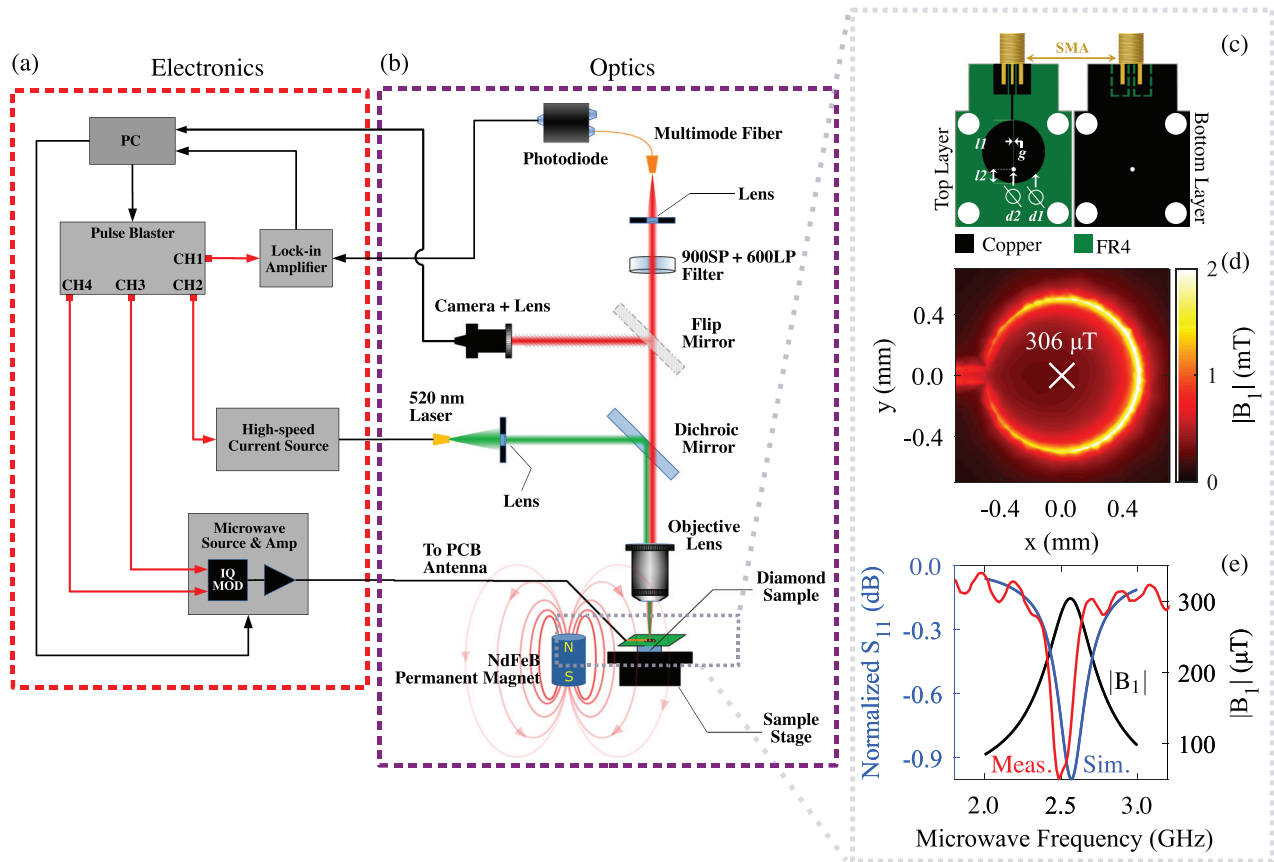
Fig. 2. (Color online) (a) Electronics setup. (b) Optics setup. (c) CAD drawing of the PCB antenna designed to deliver the oscillating magnetic field B_1 to the NV$^-$ spins. The geometric parameters are $d1 = 14$ mm, $d2 = 1.0$ mm (for laser pass-through), $l1 = 10.9$ mm, $l2 = 3.1$ mm, and $g = 0.1$ mm. The bottom layer copper is shorted to the ground/shield of the SMA connector (not shown). The design is adapted from Ref. 14, and commercially fabricated on a 0.254 mm thick FR4 substrate with 36 μm of copper thickness on each side. (d) Magnitude of the magnetic field $|B_1|$ at +24 dBm of excitation at 2.57 GHz, around the 1 mm hole. Simulations were performed in CST Microwave Studio. (e) Comparison of simulated (labeled "Sim.," left axis) and measured (labeled "Meas.," left axis) power reflected from the antenna (S_{11}), and simulated magnetic field magnitude $|B_1|$ (right axis).

The PL signal from the diamond sample is transmitted through the dichroic mirror and into the detection part of our setup. Here, a flip-mirror (Thorlabs PF10-03-P01 on Thorlabs TRF90/M) allows the signal to follow one of two paths:

(1) Through an achromatic doublet (Thorlabs AC254-125-A) onto a CMOS camera (Thorlabs DCC1545M) that allows for alignment of the sample and focusing of the laser using the 3-axis stage. A 600 nm longpass filter (Thorlabs FEL0600) and a 900 nm shortpass filter (Thorlabs FES0900) can be added here to view the PL signal instead of residual laser light.

(2) Via two silver-coated mirrors (Thorlabs PF10-03-P01) on separate kinematic mounts (Thorlabs KM100) and through an aspheric lens (Thorlabs C260TMD-B) into a 50 μm multi-mode fiber (Thorlabs M42L01) that guides the light to a photodiode (Thorlabs DET025AFC/M) for detection. A 600 nm longpass filter (Thorlabs FEL0600) and 900 nm shortpass filter (Thorlabs FES0900) are placed in this path to ensure that only the NV$^-$ PL is detected.

C. Microwave setup

A block diagram of the electronics part of our setup is shown in Fig. 2(a). The block labeled "Microwave Source &

Amp" is discussed in this section. First, a PC communicates with the MW source (SignalCore SC800) to set the MW frequency between 0 and 6 GHz. The MW signal is fed into an I/Q modulator (Texas Instruments TRF370417EVM). The I ("in-phase") input of the modulator controls the amplitude of a MW signal that has the same phase as the input MW signal. The Q ("quadrature") input controls the amplitude of a MW signal that is 90° phase-shifted. The output of the modulator is the sum of these signals. For our experiments, it is sufficient to restrict the I and Q inputs to high/low signals (TTL high or low), which enable or disable the I and Q signal components. The modulator's output is therefore either a signal that is in-phase with the input MW signal (I high, Q low), 90° out of phase (I low, Q high), or 45° out of phase (I high, Q high). The modulator's output is then amplified by a MW amplifier (ZQL-2700MLNW+) to a MW power of +24 dBm (251 mW), and transmitted to the PCB antenna [shown in Fig. 2(c)] via a coaxial cable with SMA connectors on both ends.

The antenna is designed to produce the oscillating magnetic field B_1 at the position of the NV$^-$ centers. Figure 2(c) shows our antenna design with all geometrical parameters, adapted from Ref. 14. The antenna was designed and simulated in-house using *Eagle CAD* and *CST MW Studio*, respectively, and manufactured commercially by the PCB manufacturer *Circuit Labs*. The antenna geometry is referred to as a loop-gap resonator, where the "loop" in our case is a

through hole, near which we can have a strong oscillating B_1 field in the direction perpendicular to the plane of the PCB as shown in Fig. 2(d). This hole also allows for both the excitation laser and the PL of the diamond sample to pass through the PCB.

Simulations predict that the antenna has a resonance at 2.57 GHz, indicated by the minimum of the S_{11} reflection coefficient, shown by the curve labeled "Sim." in Fig. 2(e). In the manufactured PCB, we measure the resonant S_{11} minimum to be at $\sim$2.49 GHz (curve labeled "Meas."), which agrees well with our simulated value.[20] The simulations also predict that with a MW power of +24 dBm (251 mW), the antenna produces a maximum oscillating magnetic field of $B_1 = 306\,\mu$T, which would result in an electron spin Rabi frequency of $\Omega_R = 1/2\gamma_e B_1 \approx 4.3$ MHz.[21] The diamond sample is placed as close to the top layer [Fig. 2(c)] of the PCB as possible (using tape as adhesive), and we align the excitation laser's focal spot to the center of the hole, where we can expect the greatest homogeneity of B_1 in magnitude ($||\nabla B_1|| = 0.13\ \mu$T/$\mu$m at +24 dBm of excitation power). While the antenna response peaks at $\sim$2.49 GHz, the bandwidth of the antenna is broad enough to perform the spin resonance measurements at 2.87 GHz (i.e., at $B_0 = 0$ T), which will be discussed in Sec. V B.

D. Pulsing sequences and lock-in detection

As discussed in Sec. III, the NV$^-$ center emits $\sim$30% more photons when decaying from the $|0\rangle_e$ states compared to the $|\pm1\rangle_e$ states. Under experimental conditions, where we collect emission from the four different NV$^-$ orientations simultaneously, and spin control of the ensemble is far from ideal, the contrast of the spin signal is limited to a few percent. It is possible to extract the spin signal by using a power-stabilized laser source and sufficient averaging. However, to achieve a more robust implementation for a teaching lab, we employ a lock-in amplifier.

The operation of a phase-sensitive lock-in amplifier is well-known, and described in Ref. 22. Given a reference frequency, the lock-in amplifier will make a phase-sensitive measurement of signals present exactly at that frequency, with a bandwidth as narrow as 0.01 Hz (selectable). If the signal of choice can be modulated at the reference frequency, the lock-in amplifier can extract it with a good signal-to-noise ratio (SNR) from large background signals at other frequencies. For example, in an experiment where laser excitation provides a PL signal from an ensemble of NV$^-$ centers, and a resonant MW source drives the spin from the $|0\rangle_g$ state to the $|\pm1\rangle_g$ states, the spin signal can be extracted with a lock-in amplifier when the MW field is amplitude- or frequency-modulated at the reference frequency, while any DC signal is rejected.

The experiments are clocked and triggered by a Pulse Blaster ESR Pro 250 pulse pattern generator that can be programmed to generate TTL pulse sequences on up to 24 channels. For the experiments described here, we require four channels:

- "CH0" provides the reference frequency to a phase-sensitive lock-in amplifier (Ametek 5210 or alternatively Stanford Research Systems SR830).
- "CH1" pulse-modulates the 520 nm laser diode via an in-house-designed high-speed current source (discussed in Appendix B).

- "CH2" provides the I input for the I/Q modulator (discussed in Sec. IV C).
- "CH3" provides the Q input for the I/Q modulator.

We perform our experiments by programming pulse sequences onto the four channels, keeping in mind that we only modulate the signals at the lock-in reference frequency that we are interested in detecting (except for the T_1 measurements in Sec. V A). Each experiment below has a specific pulse sequence associated with it. The software programming of each pulse sequence is done on a PC using MATLAB, and the pulse blaster is configured to generate the corresponding TTL pulses via USB serial interface.

V. EXPERIMENTS

A. Spin initialization and readout $-T_1$ measurement

At room temperature, without any laser, MW excitation, or external magnetic fields, the NV$^-$ spins are completely depolarized and the spin states are very nearly equally populated, as described by a Boltzmann distribution for a two-level system with a 2.87 GHz level splitting at 300 K. Thus, all experiments discussed in this paper will start with spin initialization via an optical pulse as described above. As discussed in Sec. III, electrons decaying via the $|s\rangle$ state will be initialized into the $|0\rangle_g$ state with a high probability. Hence, continuous 520 nm laser excitation, and therefore repeated optical cycling of the dynamics discussed in Sec. III, will result in the ensemble being initialized into the $|0\rangle_g$ state.

Readout of the NV$^-$ spin states at the end of the experiment relies on the same process. A laser pulse is used to excite the NV$^-$ centers to the $|e\rangle$ state. As relaxation via the $|s\rangle$ state is more likely for the $|\pm1\rangle_e$ state than for the $|0\rangle_e$ state, the $|0\rangle_e$ state will result in a larger number of photons being detected at the wavelengths of the ZPL and PSB.

The spin T_1 decay time gives an idea of how long the spins remain in the prepared state, before longitudinal relaxation into a Boltzmann-distributed population occurs. Note, that a T_1 experiment measures the spin decay time only, and is not sensitive to any dephasing of the system. There are two methods to measure the spin T_1 decay time:

(1) By initializing the spins into the $|0\rangle_g$ state using a laser pulse, leaving them to relax for a time τ_{delay}, and then measuring the resultant spin population with a second laser pulse. This is a fairly simple measurement that requires no MW control and works at zero B_0 magnetic field. Furthermore, it results in a signal from all members of the ensemble, irrespective of the orientation of the NV$^-$ axes.

(2) By additionally using a resonant MW pulse to coherently invert the spin population before the decay period τ_{delay}. At non-zero B_0 field, this method allows the selection of a specific spin transition and measurement of its corresponding T_1 time. However, due to the different orientations of the NV$^-$ center axes with respect to the B_0 and B_1 fields (see also Sec. III), a MW pulse will not be resonant with all the defects or lead to non-perfect inversion, producing a partial initialization of the spin ensemble and resulting in a smaller signal.

We choose the first method for the teaching labs. This method results in a stronger signal, and allows the
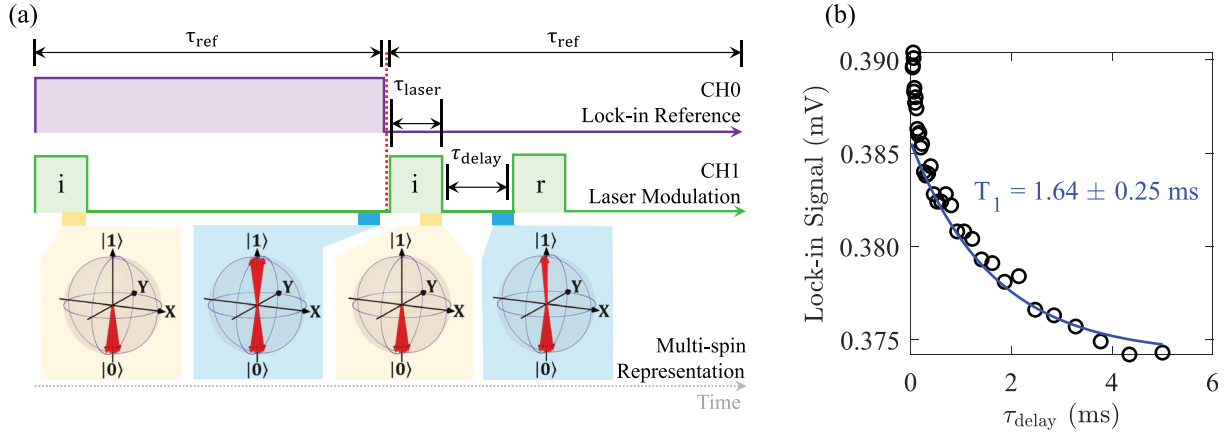
Fig. 3. (Color online) (a) Pulse sequences programmed to measure the spin T_1 decay of the NV$^-$ ground state, and a multi-spin representation showing the set of pure spin state vectors that constitute the NV$^-$ spin ensemble at selected times along the pulse sequence. $\tau_{ref}=15$ ms, $\tau_{laser}=5$ μs, and τ_{delay} is varied. (b) NV$^-$ center T_1 decay measured with lock-in detection. The total measurement time is ~3 min.

introduction of spin initialization and readout independent of the concept of MW spin control.

Figure 3(a) describes the pulse sequence to implement the all-optical T_1 measurement. CH0 sets the reference signal for the lock-in amplifier, while CH1 defines the laser pulse sequence. There are two initialization laser pulses in the sequence [denoted "i" in Fig. 3(a)], one at the beginning of each half-cycle. As they are separated by a π-phase shift with respect to the lock-in reference (CH0), the lock-in detection will cancel out this signal under the condition that $\tau_{ref} \gg T_1$. The second initialization pulse is followed by a readout laser pulse (denoted "r") of the same length, after a variable delay τ_{delay}. The signal caused by the readout pulse is dependent on the T_1 process, however since this laser pulse is only present in the second half-cycle of the reference, the readout pulse will additionally result in the detection of a PL signal that is independent of T_1 (i.e., a background signal). In Fig. 3(b), we show the corresponding measurement. The signal decreases from 0.391 mV to 0.374 mV with a time constant of $T_1 = 1.64 \pm 0.25$ ms. The 4.3% change in signal corresponds to the spin decay from the $|0\rangle_g$ state to the Boltzmann-distributed population. The 0.374 mV offset originates from the spin-independent PL signal caused by the readout pulse being present in only one of the two half-cycles.

B. Optically detected magnetic resonance and Zeeman effect

As discussed in Sec. III, an oscillating magnetic field B_1 can be used to controllably rotate the NV$^-$ ground-state electronic spin. To demonstrate this, we employ another channel of the Pulse Blaster (denoted "CH2") to pulse-modulate the output of the MW source and create a sequence of oscillating B_1 pulses, as shown in Fig. 4(a) (see also Secs. IV C and IV D for details of the setup). We start by measuring the spin transition spectrum of the NV$^-$ center ensemble in zero magnetic field. As before, an initial laser pulse is used to initialize the NV$^-$ into the $|0\rangle$ state. A subsequent MW pulse of fixed length τ_{mw} ($\gg T_2^*$) then attempts to rotate the spins. When the MW frequency is equal to the $|0\rangle_g \leftrightarrow |\pm 1\rangle_g$ transition frequency, we rotate the spins about the $+X$ axis.[23] The next laser pulse will serve as the readout pulse. This procedure is referred to as

optically detected magnetic resonance (ODMR), as the optical signal is reduced in magnitude when the spins are rotated from the $|0\rangle_g$ state into the $|\pm 1\rangle_g$ state. Using a lock-in amplifier, the resonance condition will result in a large, positive magnitude reading, which represents the absolute value of the change in signal under resonance. Out of resonance the MW pulses have no effect on the lock-in magnitude. Figure 4(b) shows the zero magnetic field ODMR spectrum. The main peak is centered at $D = 2.87$ GHz, with a spin-strain splitting $E = 7$ MHz which lifts the degeneracy of the $|0\rangle_g \leftrightarrow |\pm 1\rangle_g$ transition. Additionally, the side peaks visible are a result of hyperfine interaction ($A = 128$ MHz) of the subset of NV$^-$ spins that are also coupled to a nearest neighbor C^{13} nucleus. The side peaks are ~3.3% of the center peak intensity, which corresponds to the probability of finding a C^{13} nucleus next to an NV$^-$ site.

Figure 4(c) shows further ODMR spectra recorded for arbitrary magnetic fields B_0^A, B_0^B, B_0^C, introduced by placing a permanent magnet in the proximity of the diamond crystal. The energy splitting of the $|\pm 1\rangle_g$ state depends on the orientation of the B_0 field with respect to the NV$^-$ axis, allowing us to distinguish between the four different NV$^-$ orientations in our ODMR spectra, and resolving a total of eight transitions for the field strengths B_0^A and B_0^C, and six transitions in B_0^B due to an overlap of two pairs of transitions (see also Sec. III).

C. Rabi oscillations

The term *Rabi oscillations* refers to the driven evolution of a two-level system that manifests as the circular movement of the system's state vector around the Bloch sphere.[6] Successful demonstration of Rabi oscillations means that we have achieved coherent control, an important step in demonstrating the viability of any quantum system (see also Sec. II). Figure 4(d) shows a detailed ODMR spectrum of the $|0\rangle_g \leftrightarrow |-1\rangle_g$ transition for B_0^C. For this particular field, we have roughly aligned the magnetic field from the permanent magnet such that its direction is parallel to one of the three $[1\bar{1}\bar{1}]$, $[\bar{1}1\bar{1}]$, $[\bar{1}\bar{1}1]$ NV$^-$ center axes, and from matching the spectrum in Fig. 4(c) to theory, we can extract $B_0 = 14.2$ mT with an angle of $13.6°$ to the best-aligned NV$^-$ axis
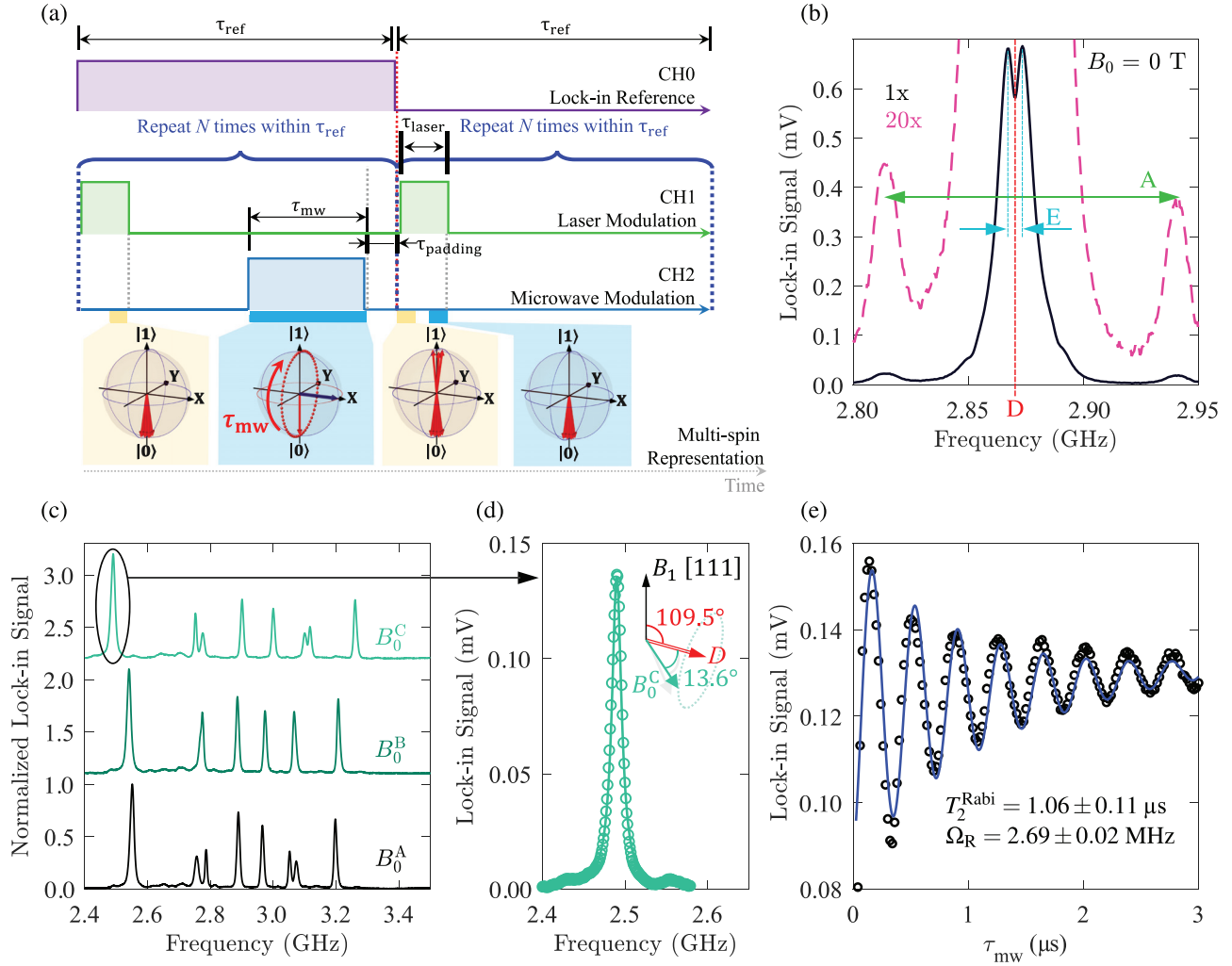
Fig. 4. (Color online) (a) Pulse sequence to perform pulsed-ODMR spectroscopy and Rabi oscillations, and multi-spin representation showing the set of pure spin state vectors on a Bloch sphere for NV$^-$ centers of one particular orientation (i.e., all spins are resonant with the MW frequency). $\tau_{ref} = 2.5$ ms, $\tau_{laser} = 5$ μs, $\tau_{padding} = 1$ μs, $\tau_{mw} = 5$ μs for pulsed-ODMR, and τ_{mw} is varied for Rabi oscillations. Laser and MW pulses sequences (CH1 and CH2) are repeated $N = 250$ times within each half-cycle to increase the signal strength. (b) Zero-field pulsed-ODMR spectrum. The main ODMR peak is centered at $D = 2.87$ GHz. The splitting $E = 7$ MHz is a result of lifting the $|\pm1\rangle_g$ degeneracy due to a spin-strain interaction [corresponding term not included in Eq. (1)]. The smaller side peaks are split by $A = 128$ MHz, and are due to the hyperfine interaction of the NV$^-$ centers coupled to a nearest neighbor C^{13} nucleus with a nuclear spin of $\pm1/2$ [corresponding term not included in Eq. (1)]. The total measurement time is $\sim$2 min. (c) Pulsed-ODMR signal obtained with a permanent magnet placed in 3 arbitrary locations within the vicinity of the sample. The B_0 magnitudes follow $B_0^A < B_0^B < B_0^C$. The total measurement time is $\sim$6 min for each magnet position. (d) Peak from (c) for B_0^C at the resonant frequency of the MW antenna [compare Fig. 2(d)]. The peak fits to a Lorentzian centered at $\nu_{ODMR} = 2.49$ GHz and linewidth $\Gamma_{FWHM} = 14.2$ MHz. (e) Rabi oscillations with MW frequency set to $\nu_{ODMR} = 2.49$ GHz. Measurement time is $\sim$8 min.

(see Fig. 4(d) inset). Furthermore, the position of the permanent magnet was adjusted such that the $|0\rangle_g \leftrightarrow |-1\rangle_g$ ODMR transition frequency coincides with the resonant frequency of the PCB antenna (see Sec. IV C). This way, we subject our NV$^-$ spins to the largest B_1 field and hence achieve the fastest Rabi oscillation frequencies.[19] This is important as short Rabi periods compared to the driven coherence time ensure a greater number of clearly observable oscillations, allowing us to perform the multi-pulse sequences described in Sec. V D. A larger B_1 field will additionally result in an ODMR peak with the largest peak intensity and broadest linewidth.

To observe Rabi oscillations, we set the driving frequency ν_{mw} to be in resonance with the ODMR transition frequency $\nu_{ODMR} = 2.49$ GHz, and vary the MW pulse length τ_{mw} while recording the lock-in signal. We

observe oscillations in the spin signal as a function of pulse length, as shown in Fig. 4(e), indicating coherent rotations of the spin around the Bloch sphere. As we have selected only one of the eight visible transitions in Fig. 4(c), we are only coherently driving NV$^-$ centers of a single axis orientation and only from the $|0\rangle_g$ to the $|-1\rangle_g$ state. The oscillations can be fitted to an exponentially decaying sinusoid

$$V_{LI} = A \cdot \sin(2\pi \Omega_R \tau_{mw} + \phi) \cdot \exp\left(-\frac{\tau_{mw}}{T_2^{Rabi}}\right)$$
$$+ B\tau_{mw} + C, \tag{3}$$

where A is the Rabi oscillation amplitude, B is a linear term included due to an observed increase in signal with increasing τ_{mw} (possibly due to heating of the sample due at long

τ_{mw}), C is an offset, $\Omega_R = 2.69 \pm 0.02$ MHz is the Rabi frequency, $\phi = -1.24 \pm 0.09$ radians is the phase-offset ($-\pi/2$ for ideal Rabi oscillations), and $T_2^{\mathrm{Rabi}} = 1.12 \pm 0.14$ μs is the driven coherence time of the spin.[24,25] The T_2^{Rabi} coherence time describes how long the $|0\rangle_g \leftrightarrow |-1\rangle_g$ transition in the ensemble can be driven before the ensemble dephases into a mixed-state. This is due to both the inhomogeneity of the B_1 field over the region of the sample in focus, and the inhomogeneous broadening of resonance frequencies over the NV$^-$ centers being measured.

From the Rabi oscillations, we can calibrate the exact $\pi/2$- and π-pulse lengths as $\tau_{\pi/2} = 72$ ns and $\tau_\pi = 144$ ns. These pulse times will be important for the experiments in Sec. V D, where we construct dynamical decoupling pulse sequences out of $\pi/2$- and π-pulses.

D. Coherence times and dynamical decoupling

In the next experiment, we measure the coherence time T_2 of the NV$^-$ centers. T_2 is the time over which a well-defined phase relation between a quantum state and a reference clock can be preserved, before noise and coupling to the environment randomize it. Compared to quantum systems operating at colder temperatures, room temperature systems are subject to a large amount of thermal energy that leads to a particularly noisy environment. As it is much easier to contemplate practical room

temperature quantum systems than those that require complex cooling mechanisms, it becomes especially interesting to investigate their room temperature coherence times. T_2 is also one of the key metrics for comparing different quantum systems, however, as there are different definitions of T_2, it important to use the same metric when comparing different quantum systems. One such coherence time was already determined in Fig. 4(e) and is the coherence time of the system while it is driven (T_2^{Rabi}). In the following experiments, we look at the coherence time during free precession of the spins using different dynamical decoupling sequences.

Dynamical decoupling methods make use of refocusing pulses, as in the Hahn-echo sequence[26] [see also Fig. 5(a)], to refocus the phases of spins that precess at slightly different rates. Here, one differentiates between inhomogeneous dephasing, where the transition frequencies of individual NV$^-$ centers are shifted due to their local environments, e.g., due to static inhomogeneities in the sample itself or in the applied B_0 magnetic field, and homogeneous dephasing where the transition frequencies of all NV$^-$ centers are broadened by similar amounts, e.g., due to dynamic noise or the finite lifetime of the quantum state. Sequences consisting of refocusing pulses are very good at refocusing static shifts in transition frequencies—a single refocusing pulse (as in the Hahn echo) is sufficient to decouple the quantum system from static noise.[26] Noise of any frequency is refocused as
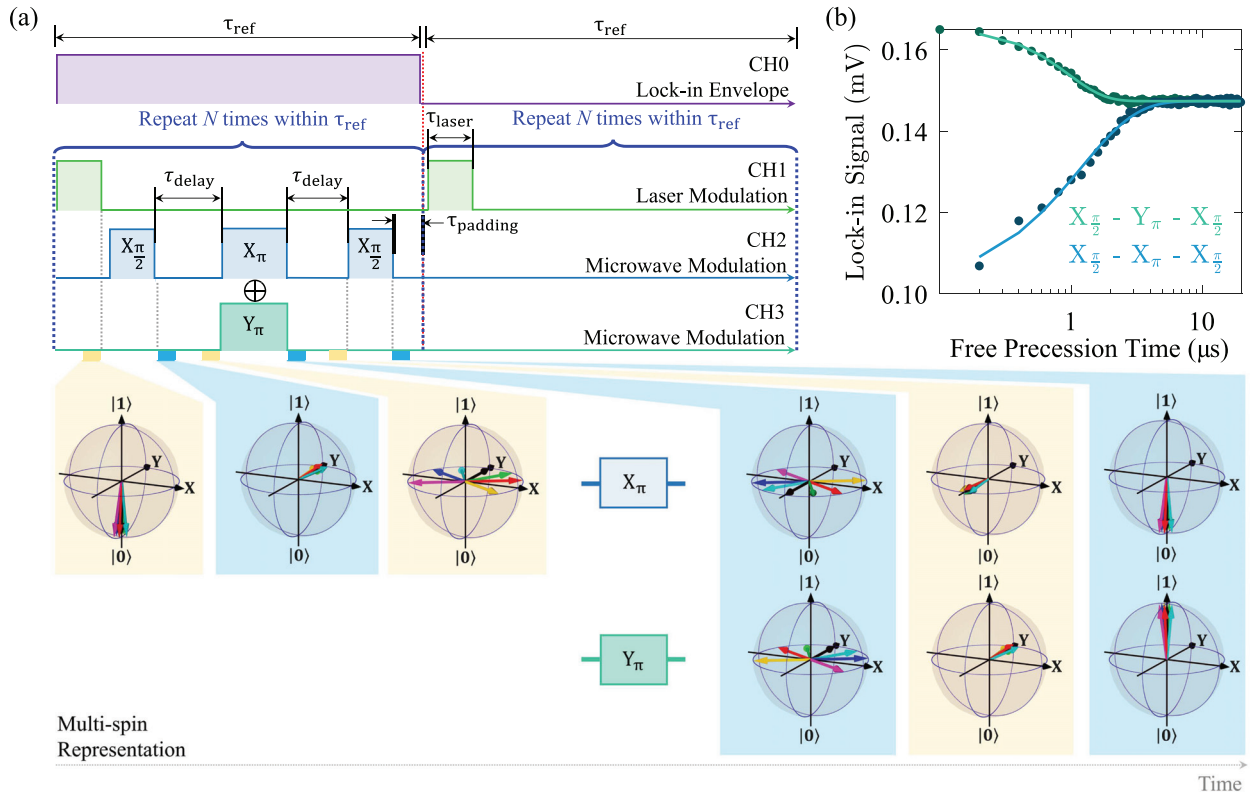
Fig. 5. (Color online) (a) Dynamical decoupling pulse sequence, with one refocusing pulse, where either a X_π-pulse, or Y_π-pulse can be chosen as the refocusing pulse. τ_{delay} is varied, and the experiment is performed under the same experimental conditions as in Fig. 4(e), with $\tau_{\pi/2} = 72$ ns and $\tau_\pi = 144$ ns. Laser and MW pulses sequences (CH1, CH2, CH3) are repeated $N = 100$ times within each half-cycle to increase the signal strength. The multi-spin representation shows the evolution of a set of pure spin state vectors on the Bloch sphere throughout the sequence. (b) Coherence time measurement for the echo sequence as in (a) with the MW π-pulse applied along the +X (Hahn echo) or +Y axis (1-pulse CPMG). For long free precession times, the ensemble enters a mixed state, as can be seen from the convergence of the two spin signals to a common value. The solid lines are fits to an exponential decay. Measurement time is ~4 min for each scan.

long as its frequency is much lower or much higher than the refocusing pulse repetition frequency, which can be best understood in the filter function formalism as described in Refs. 27 and 28. In fact, changing the pulse repetition frequency changes the frequency spectrum the spin remains sensitive to, which allows conducting detailed investigations of the noise spectrum.[28–31]

In Fig. 5(a), we show the pulse sequence used to measure the Hahn echo coherence time T_2^{Hahn}, while the Bloch spheres at the bottom of the panel give an indication of the spin orientations at specific points of the sequence. A first $X_{\pi/2}$-pulse rotates the spin to the +Y direction on the Bloch sphere. The spins are left to freely precess for a time τ_{delay}, before a X_{π}-pulse rotates them to the -Y direction. Any phase that they might have accumulated with respect to the rotating frame until then (as indicated by the coloured arrows) will be unwound in the second free precession time τ_{delay}, before a final $X_{\pi/2}$-pulse rotates them to the +Z direction for readout. We present the corresponding experimental data in Fig. 5(b). Here, τ_{delay} is increased until any phase relation is randomized and the spin signal saturates, indicating a completely mixed state. The spin refocusing pulse can be applied along either the +X (Hahn echo) or +Y axis (using IQ modulation as described in Sec. IV C), with the system entering into the same mixed-state in either case as shown in Fig. 5(b). We fit the data to an exponential decay and extract a coherence time of $T_2^{\text{Hahn}} = 1.2 \pm 0.2$ μs.
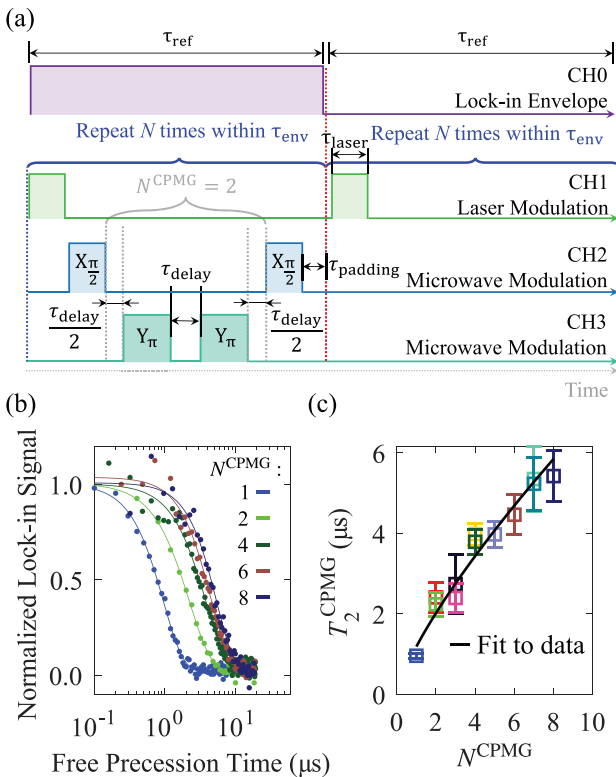
Instead of a single refocusing pulse, multiple such refocusing pulses can be applied to further extend the spin coherence time. However, performing multiple refocusing pulses about the +X axis leads to an accumulation of pulse errors. Hence, refocusing pulses about the +Y axis – known as Carr-Purcell-Meiboom-Gill (CPMG) spin-echo pulse sequence[32,33]—are more advantageous. For the CPMG pulse sequence shown in Fig. 6(a), N^{CPMG} is the total number of Y_{π}-pulses, and $t = N^{\text{CPMG}}\tau_{\text{delay}}$ is the total free precession time of the NV$^-$ spin. The CPMG pulse sequence acts as a bandpass filter, increasing the number of refocusing pulses for a fixed τ_{delay} sharpens the filter, whereas decreasing the time τ_{delay} between refocusing pulses has the effect of shifting the center of the filter to higher frequency. The bandpass center frequency is given by π/τ_{delay}.[28]

In Fig. 6(b), we plot the result of CPMG sequences with an increasing number of refocusing pulses N^{CPMG}. For the same total free precession time, a larger N^{CPMG} implies a shorter τ_{delay}, and hence a larger center frequency of the CPMG filter function.[34] The normalized lock-in signal as a function of total free precession time can be fitted to $C(t) = A \exp[(-t/T_2^{\text{CPMG}})^n]$. In Fig. 6(c), we plot the extracted T_2^{CPMG} as a function of N^{CPMG} and observe a clear correlation between $T_2^{\text{CPMG}}(N^{\text{CPMG}})$ and N^{CPMG}, suggesting that the noise spectral density of the NV$^-$ electron's environment reduces towards higher frequencies. We were able to fit these data with a function of the form $T_2^{\text{CPMG}}(N^{\text{CPMG}}) = B(N^{\text{CPMG}})^\alpha$ with $\alpha = 0.77 \pm 0.13$, which is within the bounds experimentally determined in Ref. 34 for a CVD grown diamond with a large NV$^-$ density ($\sim 10^{16}$cm^{-3}).

VI. CONCLUSION

We have presented a cost-effective experimental setup that is suitable for demonstrating coherent spin control concepts in an undergraduate teaching laboratory environment. The experiments implement the optically detected magnetic resonance technique at room temperature on NV$^-$ centers in diamond, and the setup is constructed using the minimal necessary optics and electronics components. Students will develop an intuitive feeling for quantum spin physics, gain first-hand experience in controlling a quantum system, and have the freedom to develop unique pulse sequences and observe the results in real-time. The use of a high-density NV$^-$ diamond sample provides a large signal, making the measurements insensitive to misalignment of the optics and exposure to high ambient light levels—as is desirable for an undergraduate lab setup.

Fig. 6. (Color online) (a) Pulse sequences for the CPMG spin-echo sequence, where N^{CPMG} is number of Y_{π} refocusing pulses. Laser and MW pulse sequences (CH1, CH2, CH3) are repeated $N = 100$ times within each half-cycle to increase the signal strength. (b) Examples of CPMG measurements for different N^{CPMG}. The measurement time is $\sim$4 min for each scan. (c) Extracted T_2^{CPMG} for all CPMG scans.

APPENDIX A: LIST OF PARTS

Table I. List of parts for "Optics" section of experimental set-up, shown in Fig. 2(b).

Item	Supplier	Part number	Application	Price (USD) (December 17, 2019)	Qty	Total (USD)
Housing						
Aluminum Breadboard	Thorlabs	MB3045/M	Base plate	199.45	1	199.45
Enclosure	Thorlabs	XE25C7/M	Enclosure for all optics	199.11	1	199.11
Optical Excitation						
SM Fiber-Pigtailed Laser Diode	Thorlabs	LP520-SF15	Excitation laser	717.45	1	717.45
Laser Diode ESD Protection	Thorlabs	SR9HA	Laser diode protection	54.11	1	54.11
Fiber Adapter Plates	Thorlabs	SM1FC - FC/PC	Laser fiber coupling	31.38	1	31.38
Kinematic Mount	Thorlabs	KM100T	Laser mounting	70.87	1	70.87
50 mm Pedestal Pillar Post	Thorlabs	RS2P/M	Laser mounting	28.95	1	28.95
Aspheric Lens	Thorlabs	C280TMD-A	Laser collimation lens	85.49	1	85.49
SM1 to M9 Lens Cell Adapter	Thorlabs	S1TM09	Lens mounting	24.35	1	24.35
SM1 Lens Tube 1.50in	Thorlabs	SM1L15	Lens mounting	16.17	1	16.17
Longpass 550 nm dichroic mirror	Thorlabs	DMLP550	Excitation/detection filtering	182.88	1	182.88
Kinematic Mount	Thorlabs	KM100	Dichroic mirror mount	39.86	1	39.86
50 mm Pedestal Pillar Post	Thorlabs	RS2P/M	Dichroic mirror mount	28.95	1	28.95
Microscope Objective	Olympus	MS Plan 50×/0.80NA	Excitation lens	744	1	744
RMS Threaded Cage Plate	Thorlabs	CP42/M	Objective lens mount	32.78	1	32.78
50 mm Pedestal Pillar Post	Thorlabs	RS2P/M	Objective lens mount	28.95	1	28.95
5 mm Post Spacer	Thorlabs	RS5M	Objective lens mount	8.17	1	8.17
Sample Mount						
3-axis Sample Positioner	Thorlabs	MBT616D/M	Stage for diamond sample	1184.92	1	1184.92
Blank Device Mount	Thorlabs	HBB002	Sample mount	56.55	1	56.55
Imaging						
Protected Silver Mirror	Thorlabs	PF10-03-P01	Imaging mirror	53.58	1	53.58
Flip Mount	Thorlabs	TRF90/M	Mirror mounting	88.73	1	88.73
38 mm Pedestal Pillar Post	Thorlabs	RS1.5P4M	Mirror mounting	25.21	1	25.21
600 nm Longpass Filter (optional)	Thorlabs	FEL0600	Imaging filtering	80.62	1	80.62
900 nm Shortpass filter (optional)	Thorlabs	FES0900	Imaging filtering	80.62	1	80.62
SM1 Lens Tube 0.50in (optional)	Thorlabs	SM1L05	Filter mounting	12.97	2	25.94
Achromatic Doublet	Thorlabs	AC254-125-A	Imaging lens	81.16	1	81.16
SM1 Lens Tube 1.50in	Thorlabs	SM1L15	Lens mounting	16.17	1	16.17
CMOS Camera	Thorlabs	DCC1545M	Imaging camera	387.92	1	387.92
SM1 Lens Tube Spacer 3.50in	Thorlabs	SM1S35	Lens/camera mounting	25.53	1	25.53
SM1 Cage Plate	Thorlabs	CP33/M	Lens/camera mounting	16.89	2	33.78
50 mm Pedestal Pillar Post	Thorlabs	RS2P/M	Objective lens mount	28.95	2	57.9
5 mm Post Spacer	Thorlabs	RS5M	Objective lens mount	8.17	2	16.34
Detection						
Protected Silver Mirror	Thorlabs	PF10-03-P01	Detection mirror	53.58	2	107.16
Kinematic Mount	Thorlabs	KM100	Mirror mounting	39.86	2	79.72
50 mm Pedestal Pillar Post	Thorlabs	RS2P/M	Mirror mounting	28.95	2	57.9
600 nm Longpass Filter	Thorlabs	FEL0600	Detection filtering	80.62	1	80.62
900 nm Shortpass filter	Thorlabs	FES0900	Detection filtering	80.62	1	80.62
SM1 Lens Tube 0.50in	Thorlabs	SM1L05	Filter mounting	12.97	2	25.94
Aspheric Lens	Thorlabs	C260TMD-B	Fiber coupling lens	85.49	1	85.49
SM1 to M9 Lens Cell Adapter	Thorlabs	S1TM09	Lens mount	24.35	1	24.35
XY-Axes Translation Mount	Thorlabs	ST1XY-D/M	Fiber alignment	517.26	1	517.26
38 mm Pedestal Pillar Post	Thorlabs	RS1.5P4M	Fiber coupler mounting	25.21	1	25.21
4 mm Post Spacer	Thorlabs	RS4M	Fiber coupler mounting	7.9	1	7.9
Z-Axis Translation Mount	Thorlabs	SM1Z	Fiber alignment	205.6	1	205.6
2-inch Rods	Thorlabs	ER2	Fiber alignment	6.28	4	25.12
Fiber Adapter Plates	Thorlabs	SM1FC - FC/PC	Fiber coupling	31.38	1	31.38
50 micron FC/PC Multimode Fiber	Thorlabs	M42L01	Detection fiber	70.87	1	70.87

Table I. (*Continued*)

Item	Supplier	Part number	Application	Price (USD) (December 17, 2019)	Qty	Total (USD)
Si Photodetector	Thorlabs	DET025AFC/M	Signal detection	306	1	306
Mounting M6 Clamping Fork	Thorlabs	CF125C/M	Mounting	11.69	9	105.21
Sample CVD Diamond Sample (e.g., SC Plate CVD ⟨100⟩)	Element Six	145–500-0274–01	Sample	130	1	130
B0 and B1 Magnetic Fields PCB Antennas (pack of 5)	Circuit Labs		B1 Microwave Excitation	72.16	1	72.16
Neodymium Block Magnets $10 \times 10 \times 5$ mm	AMF Magnets		B0 Static Magnetic Field	2.3	4	9.2
Total Optics Cost:						6780.6

Table II. List of parts for "Electronics" section of experimental set-up, shown in Fig. 2(a).

Item	Supplier	Part number	Application	Price (USD) (December 17, 2019)	Qty	Total (USD)
USB Pulse Blaster	SpinCore	PBESR-PRO-250-USB	Pulse Sequences	4485	1	4485
Dual Phase Lock-In	Ametek	5210	Lock-in detection	2000	1	2000
Windows PC				2000	1	2000
6 GHz Microwave Source	SignalCore	SC800	Microwave Drive	1295	1	1295
Benchtop 3-Channel PSU	Newark	HM7042-5.02	Microwave Drive Power	1155	1	1155
RF Amplifier	Mini-Circuits	ZQL-2700MLNW+	Microwave Drive	304.95	1	304.95
IQ Modulator	Texas Instr.	TRF370417EVM	Microwave Drive	199	1	199
12V DC Wall Adapter	Thorlabs	LDS12B	Home-built current source	85.22	1	85.22
RS232 Serial Adapter	StarTech	ICUSB232DB25	Lock-in detection	20.99	1	20.99
BNC-BNC Coaxial	Thorlabs	2249-C-48	TTL Signals	19.29	5	96.45
SMA-SMA Coaxial 12-inch	Thorlabs	CA2912	Microwave interconnects	15.69	4	62.76
SMA 50-ohm termination	Mini-Circuits	ANNE-50X	IQ Modulator	15.95	2	31.9
BNC-SMA Adapter	Thorlabs	T4290	IQ Modulator	14.07	2	28.14
USB A-Mini B Cable	Thorlabs	USB-AB-72	Microwave Source	8.87	1	8.87
USB A-B Cable	Thorlabs	USB-A-79	Pulse Blaster	8.87	1	8.87
BNC-Banana Adapter	Thorlabs	T1452	Laser Diode ESD Protection	8.65	1	8.65
Banana Patch Cable	Thorlabs	T13120(2)	Microwave Drive Power	7.31	4	29.24
Total Electronics Cost:						11820.04

APPENDIX B: DESIGN OF THE LASER DRIVER

Table III. List of parts required to assemble current driver circuit in Fig. 7.

Component	Description	Supplier	Part number	Price (USD) (December 17, 2019)	Qty	Total (USD)
U1	LDO 3V3 Regulator	Element 14	1469102	1.6	1	1.6
U2	Integrated Power Supply	RS Online	798–1290	19.05	1	19.05
U3	Current Source	RS Online	779–9615	5.58	1	5.58
J1 J3 J4	BNC Connector	Element 14	1169739	7.25	3	21.75
J2	Barrel Jack	Element 14	1854514	1.25	1	1.25
Q1	PFET	Element 14	1510765	0.27	1	0.27
Q8	NFET	Element 14	2317616	0.2	1	0.2
Q6	Dual NFET	Element 14	2706719	1.07	1	1.07
R1	1 kΩ Resistor 0603	Element 14	2284191	0.14	1	0.14
R3	16.5 kΩ Resistor 0805	Element 14	2483960	0.46	1	0.46

Table III. (*Continued*)

| Component	Description	Supplier	Part number	Price (USD) (December 17, 2019)	Qty	Total (USD)
R4	1 Ω Resistor 0805	Element 14	2813642	0.31	1	0.31
R5	10 kΩ Resistor 0603	Element 14	1652827	0.19	1	0.19
R6	205 kΩ Resistor 0603	Element 14	2303251	0.01	1	0.01
R7	75 kΩ Resistor 0603	Element 14	1799354	0.01	1	0.01
R8	102 kΩ Resistor 0603	Element 14	2336927	0.21	1	0.21
C1 C4	10 μF Capacitor 1206	Element 14	2118134	0.61	2	1.22
C2 C3 C7	1 μF Capacitor 0603	Element 14	1845736	0.16	3	0.48
C6 C8 C9 C10 C11	100 μF Capacitor 0603	Element 14	1709958	0.02	5	0.1
C5	100 μF Capacitor 0603	Element 14	2354734	1.57	1	1.57
PCB		Seeed Studio		57.86	1	57.86
Total PCB Cost:						113.33
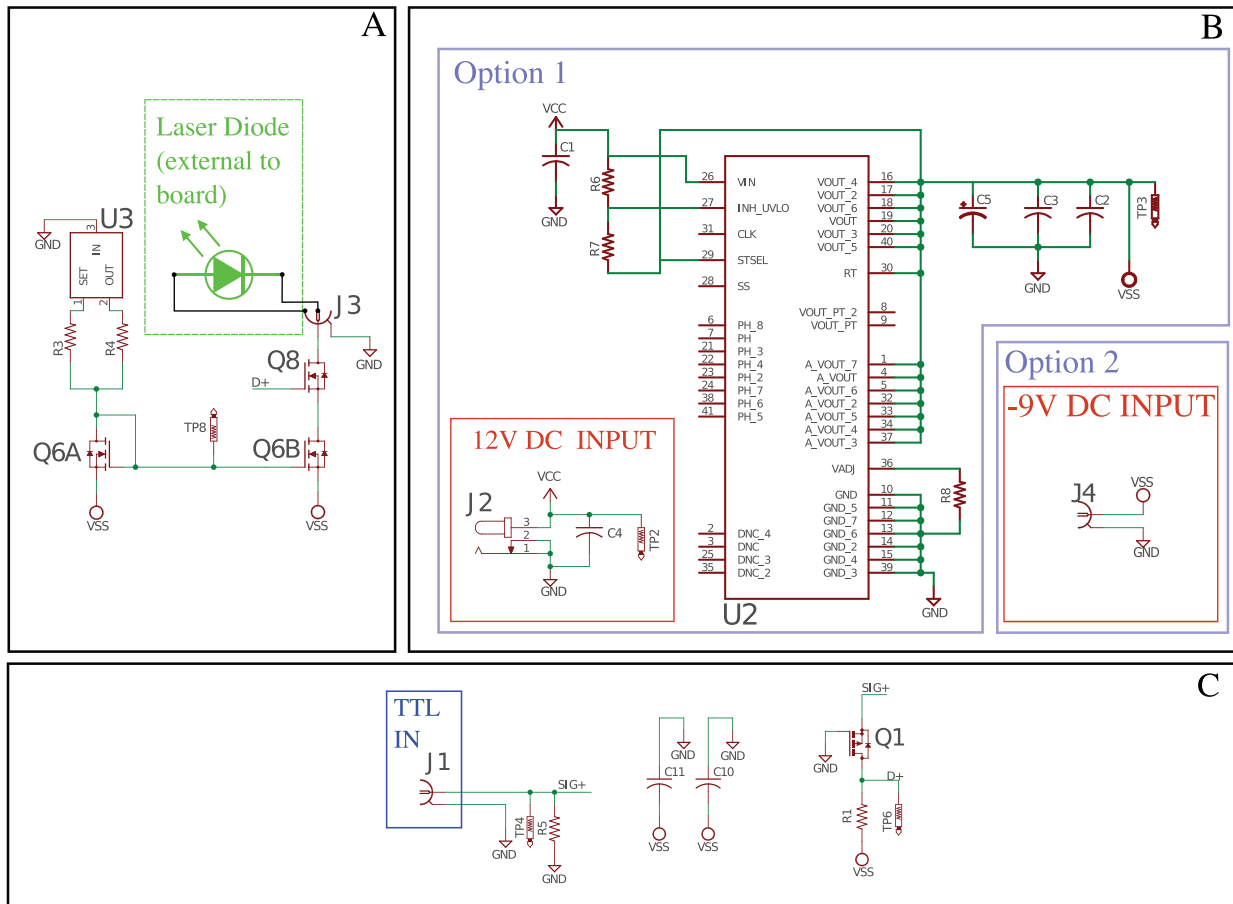
Fig. 7. (Color online) Schematic of the custom current source used in this experiment, broken down into the three main blocks. (a) The circuitry supplying the current to the diode. U3 is an off-the-shelf current source integrated circuit that has the output current set by R3 and R4 to ∼165 mA. As U3 requires some time to settle to a steady state current, if we were to modulate this current directly, we would not be able to operate at the desired bandwidth of 10 MHz. Thus we construct a current mirror using Q6; a matched pair of N-channel MOSFETs. The mirror sources 165 mA through the diode, unless the connection is interrupted by Q8. This allows U3 to output a constant, stable current, circumventing the switching speed problems. (b) Power supplies required for the operation of the circuit. There are two options available for the operation of this circuit. In "Option 1," an external 12 V input can be provided, which is then regulated down to Vss by U2. In "Option 2," a lab power supply can be directly connected to the circuit to provide the power. Vss was set to −9 V as a safety feature. The case of the laser diode is at the electrical potential of the anode and thus, this potential was set to ground. As a consequence, a negative supply voltage is required. For the current source that was used to obtain the results in this paper, there was a soldering error with the power supply provided by U2 in "Option 1," and thus "Option 2" was used. We have populated another PCB with "Option 1" for another teaching setup and confirmed that it functions correctly. (c) Input logic and a level shifter. This block takes the TTL input signal and level-shifts it between ground and Vss. Such voltage levels are required to correctly drive the MOSFETs in block (a), as standard TTL levels would not be able to switch Q8 due to the presence of negative supply voltages.
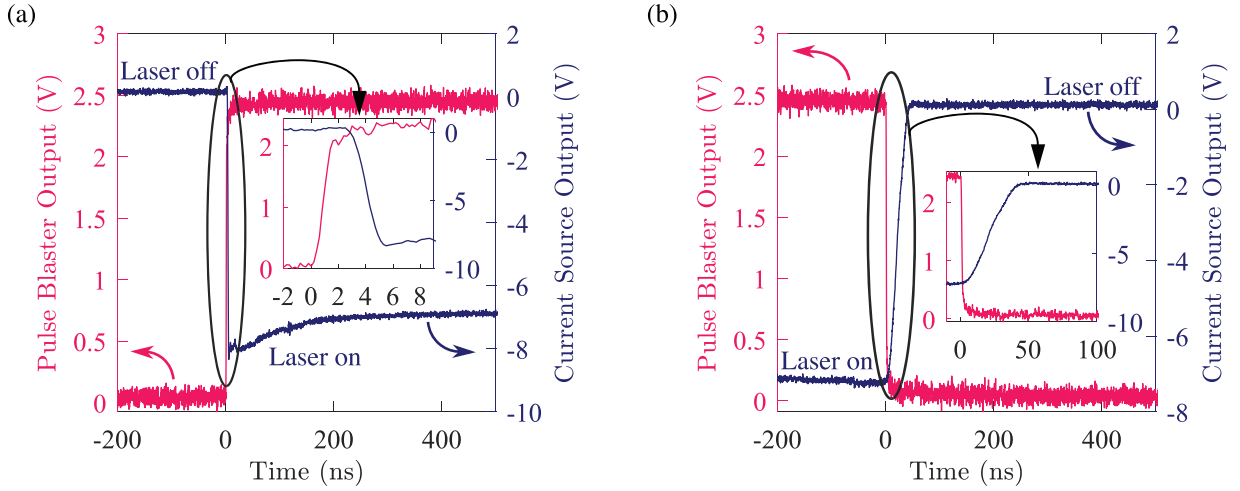
Fig. 8. (Color online) (a) and (b) Performance characterization of the current driver, showing (a) turn-on and (b) turn-off of the laser. The curve corresponding to the left axis is a copy of the pulse blaster TTL output that is used as an input for the current driver. The curve corresponding to the right axis is the output of the current driver at its (a) falling edge and (b) rising edge, respectively. The traces were measured with a Tektronix TDS3052 oscilloscope with 250 MHz bandwidth. The input impedances of both oscilloscope channels were $50 \sim \omega$. The fall time of the current source output (turn-on time) is 1.6 ns and the rise time (turn-off time) is 27.0 ns.
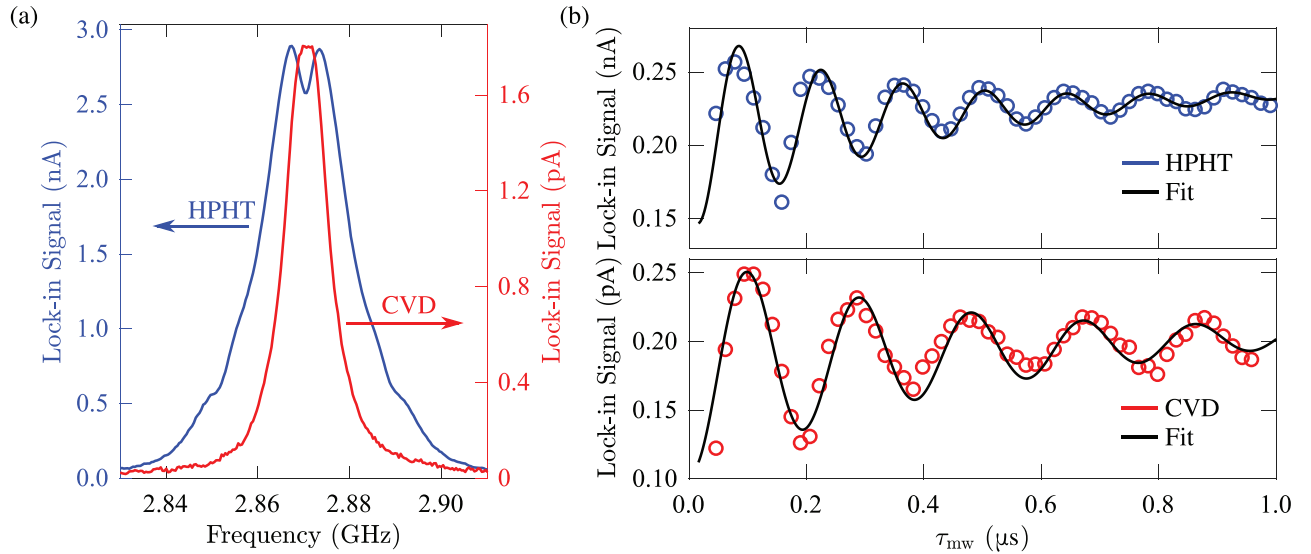
APPENDIX C: COMPARISON OF HPHT AND CVD DIAMOND

Fig. 9. (Color online) Measurements comparing the HPHT diamond used for all experiments in the main text and a CVD diamond purchased from *Element Six*, listed in Appendix A. Measurements were taken in current mode (similar signal-to-noise ratios were observed for voltage and current mode) of the EG&G 5210 lock-in amplifier listed in Appendix A. The PL emitted was 705 nW by the HPHT diamond and 0.75 nW by the CVD diamond, as measured with a power meter for ~15 mW excitation power at $\lambda_{\text{exc}} = 520$ nm. (a) Zero-field ODMR comparison. Measurement time was ~2 min for the HPHT diamond and ~9 min for the CVD diamond for a spectrum with 200 data points. (b) Rabi oscillations comparison at $\nu_{\text{ODMR}} = 2.53$ GHz. Measurement time was ~2 min for the HPHT diamond and ~13 min for the CVD diamond for 60 data points. Fits were performed with Eq. (3), which gives $T_2^{\text{Rabi}} = 310 \pm 60$ ns and $\Omega_R = 7.2 \pm 0.1$ MHz for the HPHT diamond, and $T_2^{\text{Rabi}} = 450 \pm 90$ ns and $\Omega_R = 5.2 \pm 0.1$ MHz for the CVD diamond. In these measurements, T_2^{Rabi} is limited by the inhomogeneous broadening of the ensemble linewidth, e.g., due to strain and hyperfine coupling to nuclear spins, and the inhomogeneity of the B_1 field. The PCB antenna used to perform these measurements had the same dimensions as described in Fig. 2(c), except with the center hole diameter $d = 0.6$ mm, different from the $d2 = 1.0$ mm used in the main text. While a smaller hole delivers a larger B_1 field (hence increasing Ω_R), a shorter T_2^{Rabi} is expected due to the increased inhomogeneity of the B_1 field at the center of the hole. The higher Ω_R of the HPHT diamond compared to that of the CVD diamond can be explained by the different projections of the B_1 vector onto the NV$^-$ axes being measured (Ref. 19).

a)Electronic mail: v.sewani@student.unsw.edu.au

b)Electronic mail: a.laucht@unsw.edu.au

[1] J. P. Dowling and G. J. Milburn, "Quantum technology: The second quantum revolution," Philos. Trans. R. Soc. London. Ser. A: Math. Phys. Eng. Sci. **361**, 1655–1674 (2003).

[2] M. W. Doherty et al., "The nitrogen-vacancy colour centre in diamond," Phys. Rep. **528**, 1–45 (2013).

[3] H. Zhang et al., "Little bits of diamond: Optically detected magnetic resonance of nitrogen-vacancy centers," Am. J. Phys. **86**, 225–236 (2018).

[4] Qutools. Quantum sensing by diamond magnetometer <https://www.qu-tools.com/qunv/>. Accessed on March 26, 2019.

[5] D. B. Bucher et al., "Quantum diamond spectrometer for nanoscale NMR and ESR spectroscopy," Nat. Protoc. **14**, 2707–2747 (2019).

[6] T. S. Humble, H. Thapliyal, E. Munoz-Coreas, F. A. Mohiyaddin, and R. S. Bennink, "Quantum computing circuits and devices," IEEE Des. Test **36**, 69–94 (2019).

[7] T. D. Ladd and M. S. Carroll, "Silicon qubits," Encyclopedia Mod. Opt. **1**, 467–477 (2018).

[8]X. Zhang *et al.*, "Qubits based on semiconductor quantum dots," Chin. Phys. B **27**, 020305 (2018).

[9]L. M. Vandersypen and I. L. Chuang, "NMR techniques for quantum control and computation," Rev. Mod. Phys. **76**, 1037–1069 (2005).

[10]J. Clarke and F. K. Wilhelm, "Superconducting quantum bits," Nature **453**, 1031–1042 (2008).

[11]H. Häffner, C. F. Roos, and R. Blatt, "Quantum computing with trapped ions," Phys. Rep. **469**, 155–203 (2008).

[12]A. Boretti, L. Rosa, J. Blackledge, and S. Castelletto, "Nitrogen-vacancy centers in diamond for nanoscale magnetic resonance imaging applications," Beilstein J. Nanotechnol. **10**, 2128–2151 (2019).

[13]E. Abe and K. Sasaki, "Tutorial: Magnetic resonance with nitrogen-vacancy centers in diamond—Microwave engineering, materials science, and magnetometry," J. Appl. Phys. **123**, 161101 (2018).

[14]K. Sasaki *et al.*, "Broadband, large-area microwave antenna for optically detected magnetic resonance of nitrogen-vacancy centers in diamond," Rev. Sci. Instrum. **87**, 053904 (2016).

[15]See supplementary material at https://doi.org/10.1119/10.0001905 for *Eagle CAD* schematics and board layouts for PCB antenna in Fig. 2(d) and current source design in Fig. 7. Design rule checks (DRC) and generation of Gerber files should be performed according to manufacturers' instructions.

[16]R. Rubinas *et al.*, "Spin properties of NV centers in high-pressure, high-temperature grown diamond," J. Phys. Commun. **2**, 115003 (2018).

[17]Scimed. HD NV-center diamonds. <http://www.scimed.de/HDNVcenter/Frameset%20aktuell.html> Accessed on June 11, 2020.

[18]Element Six. Element Six - eShop. <https://e6cvd.com/uk/application/all.html> Accessed on June 11, 2020.

[19]Due to the geometry of the PCB antenna, the B_1 field that it generates is along [111] crystal direction. This renders it ineffective for driving magnetic resonance transitions on the [111]-oriented NV^- centers. However, for the [$1\bar{1}\bar{1}$], [$\bar{1}1\bar{1}$], [$\bar{1}\bar{1}1$]-oriented NV^- centers, B_1 is only misaligned from the optimal perpendicular configuration by $19.47°$, resulting in a 94% effective magnetic resonance drive. In the case of a $\langle 100 \rangle$-oriented diamond, such as the *Element Six* diamond described in Sec. IV A, the angle between the B_1 field and any NV^- orientation is $54.74°$, resulting in a 57.74% effective magnetic resonance drive.

[20]For ordering of the PCB antennas, it is important to choose the same substrate material (FR4) and substrate thickness (0.254 mm) as these parameters, and any other modifications in the antenna dimensions will result in a shift in the resonant frequency. A network analyzer can be used to determine the S_{11} minimum of the antenna and hence its resonance frequency. Alternatively, the ODMR peak intensity or linewidth can be carefully monitored near $\sim$2.5 GHz to determine the exact resonant frequency.

[21]The factor of 1/2 comes from the fact that we are using an oscillating, not a rotating, magnetic field.

[22]J. H. Scofield, "Frequency-domain description of a lock-in amplifier," Am, J. Phys. **62**, 129–133 (1994).

[23]By convention, the first pulse defines the rotation axis as +X.

[24]F. Yan *et al.*, "Rotating-frame relaxation as a noise spectrum analyser of a superconducting qubit undergoing driven evolution," Nat. Commun. **4**, 2337 (2013).

[25]A. Laucht *et al.*, "A dressed spin qubit in silicon," Nat. Nanotechnol. **12**, 61–66 (2017).

[26]E. L. Hahn, "Spin echoes," Phys. Rev. **80**, 580–594 (1950).

[27]M. Biercuk, A. Doherty, and H. Uys, "Dynamical decoupling sequence construction as a filter-design problem," J. Phys. B: At. Mol. Opt. Phys. **44**, 154002 (2011).

[28]J. Bylander *et al.*, "Noise spectroscopy through dynamical decoupling with a superconducting flux qubit," Nat. Phys. **7**, 565–570 (2011).

[29]G. A. Álvarez and D. Suter, "Measuring the spectrum of colored noise by dynamical decoupling," Phys. Rev. Lett. **107**, 230501–230505 (2011).

[30]J. T. Muhonen *et al.*, "Storing quantum information for 30 seconds in a nanoelectronic device," Nat. Nanotechnol. **9**, 986–991 (2014).

[31]K. Chan *et al.*, "Assessment of a silicon quantum dot spin qubit environment via noise spectroscopy," Phys. Rev. Appl. **10**, 044017 (2018).

[32]H. Y. Carr and E. M. Purcell, "Effects of diffusion on free precession in nuclear magnetic resonance experiments," Phys. Rev. **94**, 630–638 (1954).

[33]S. Meiboom and D. Gill, "Modified spin-echo method for measuring nuclear relaxation times," Rev. Sci. Instrum. **29**, 688–691 (1958).

[34]N. Bar-Gill *et al.*, "Suppression of spin-bath dynamics for improved coherence of multi-spin-qubit systems," Nat. Commun. **3**, 585–591 (2012).

Author/s:
Sewani, VK; Vallabhapurapu, HH; Yang, Y; Firgau, HR; Adambukulam, C; Johnson, BC; Pla, JJ; Laucht, A

Title:
Coherent control of NV- centers in diamond in a quantum teaching lab

Date:
2020-12-01

Citation:

Persistent Link:
http://hdl.handle.net/11343/273844

File Description:
Published version
License: